

Unfolding the Origin of the Ultrafast Optical Response of Titanium Nitride

Silvia Rotta Loria, Beatrice Roberta Bricchi, Andrea Schirato, Luca Mascaretti, Cristina Mancarella, Alberto Naldoni, Andrea Li Bassi, Giuseppe Della Valle,* and Margherita Zavelani-Rossi*

Ultrafast plasmonics is driving growing interest for the search of novel plasmonic materials, overcoming the main limitations of noble metals. In this framework, titanium nitride (TiN) is brought in the spotlight for its refractory properties combined with an extremely fast electron-lattice cooling time (<100 fs) compared to gold (≈ 1 ps). Despite the results reported in literature, a clear-cut explanation of the origin of the ultrafast and giant optical response of TiN-based materials upon excitation with femtosecond laser pulses is still missing. To address this issue, an original model is introduced, capable of unfolding the modulation of TiN optical properties on a broad bandwidth, starting from the variations of electronic and lattice temperatures following ultrafast photoexcitation. The numerical analysis is validated on ultrafast pump-probe spectroscopy experiments on a simple structure, a TiN film on glass. This approach enables a complete disentanglement of the interband and intraband contributions to the permittivity modulation. Moreover, it is also shown that, varying the synthesis conditions of the TiN film, not only the static, but also the dynamical optical response can be efficiently tuned. These findings pave the way for a breakthrough in the field: the design of TiN-based ultrafast nanodevices for all-optical modulation of light.

1. Introduction

Plasmonics is a broad, well established research subject that exploits efficient light-matter interaction to manipulate and enhance optical fields at the nanoscale.^[1–3] Among the various applications, we mention high resolution imaging, sensing, nanomedicine, information processing, surface enhanced Raman scattering, energy conversion and photocatalysis.^[4–8] Moreover, in the temporal, ultrafast regime, plasmonic systems represent a well established platform for the excitation of high-energy (hot) carriers, which have lately gained a broad interest.^[9,10] In this framework, the development of ultrafast pump-probe spectroscopy techniques, able to investigate light-matter interactions at the femtosecond (fs) timescale, offer an unparalleled channel for the study of these out-of-equilibrium electronic states.^[11] Along with the growing interest toward

S. Rotta Loria, A. Schirato, G. Della Valle
Dipartimento di Fisica
Politecnico di Milano
Piazza Leonardo da Vinci, 32, Milano I-20133, Italy
E-mail: giuseppe.dellavalle@polimi.it

B. R. Bricchi, C. Mancarella, A. Li Bassi, M. Zavelani-Rossi
Dipartimento di Energia
Politecnico di Milano
via G. Ponzio 34/3, Milano I-20133, Italy
E-mail: margherita.zavelani@polimi.it

A. Schirato
Istituto Italiano di Tecnologia
via Morego 30, Genova I-16163, Italy


A. Schirato
Department of Electrical and Computer Engineering
Rice University
Houston, TX 77005, USA

L. Mascaretti, A. Naldoni
Czech Advanced Technology and Research Institute
Regional Centre of Advanced Technologies and Materials
Palacký University Olomouc
Šlechtitelů 27, Olomouc 77900, Czech Republic

A. Naldoni
Department of Chemistry and NIS Centre
University of Turin
Turin 10125, Italy

A. Li Bassi
Center for Nano Science and Technology - IIT@PoliMi
Via Giovanni Pascoli 70/3, Milano 20133, Italy

G. Della Valle, M. Zavelani-Rossi
Istituto di Fotonica e Nanotecnologie - Consiglio Nazionale delle Ricerche
Piazza Leonardo da Vinci, 32, Milano I-20133, Italy

 The ORCID identification number(s) for the author(s) of this article can be found under <https://doi.org/10.1002/adom.202300333>

© 2023 The Authors. Advanced Optical Materials published by Wiley-VCH GmbH. This is an open access article under the terms of the Creative Commons Attribution License, which permits use, distribution and reproduction in any medium, provided the original work is properly cited.

DOI: 10.1002/adom.202300333

the ultrafast optical response of plasmonic structures, the last decade has witnessed an effort in finding new materials able to overcome the main limitations of most popular plasmonic metals, such as gold and silver.^[12,13] Indeed, though having low ohmic losses in the visible range and good DC conductivity, these metals suffer from high interband losses at optical frequencies. Other limitations include low stability at high temperatures (further worsened by melting point depression in nanostructures), incompatibility with semiconductor fabrication process flow and a non-tailorable permittivity. Even other metals, having low interband losses, are plagued by dissipation caused by high resistivity.^[12,14] Many alternative materials have been explored in the attempt of reducing metals' high carrier concentration, representing the main feature responsible for losses. Among them, doped semiconductors such as copper selenide and chalcogenides, chalcopyrite and transparent conductive oxides, and diluted metals like interstitial metal nitrides have been reported.^[14–18] In this last category, titanium nitride (TiN), has gained remarkable attention for its refractory properties,^[14] chemical stability,^[19] CMOS.^[20] and bio-compatibility.^[19] Moreover, TiN shows a broad plasmonic resonance (visible (vis)–near infra-red (NIR)) and its permittivity is tunable by acting on its stoichiometry at the synthesis stage, so that the plasmonic resonance can be spectrally adjusted.^[21,22] TiN has been exploited for example in solar-thermal conversion,^[23–28] on chip applications,^[29,30] and second harmonic generation.^[31,32] The static optical properties of TiN have been widely studied^[33–37] and its plasmonic features have been explored analytically and numerically,^[38,39] contrary to its transient response, which has been investigated only recently^[40–44] and has sparked debates on the relaxation timescales of hot electrons. Refs. [41, 42] have reported a slow thermalization with the lattice, taking place on a timescale of tens/hundreds of picoseconds, whereas, later, in refs. [43, 44] the electron–phonon coupling in TiN was found to be much higher than in other metals. Indeed, it was shown that the hot electron relaxation with the lattice takes place in less than 100 fs, namely one order of magnitude faster than, for example, in gold. However, in the above-mentioned works,^[41–44] only single-wavelength models for TiN transient optical response have been proposed. This extremely fast nonlinear dynamics is very promising for ultrafast plasmonics, to realize ultrafast all-optical modulators, based, for example, on metasurfaces.^[45–47] This material, indeed, boasts the huge hot electron nonlinearity of a metal together with an ultrafast recovery time, which could significantly increase the all-optical modulation speed. However, a complete model of the third-order nonlinearity of TiN is still missing. This turns out to be of crucial importance in view of device design, which requires a quantitative description not only of the hot carrier temporal dynamics, already provided by the two-temperature model (2TM), but also of the spectral permittivity changes driven by non-equilibrium electronic states. In this work, we aim at quantifying both the permittivity modulation induced by a pump pulse and its effect on the transient optical response of a TiN sample, on a broad spectral range. Indeed, exploiting the 2TM and inspired by the calculations already developed for gold^[48–50] and Cu_{2-x}Se ,^[51] we formulate a complete numerical model for the nonlinear optical response of TiN. The model takes into account nonequilibrium electronic and phononic populations, as well as variations of the permittivity due to interband and intra-

band modulations and due to the thermoelastic effect. We validate our results on experimental data, that we obtain by ultrafast transient reflection spectroscopy measurements, performed with < 100 fs temporal resolution and broadband probe pulses, on the simplest TiN structure, namely a polycrystalline thin film on glass. Our approach enables us to disentangle the contributions to the transient modulation of the dielectric properties, as well as to quantify them in the ultrafast timescale and on a broad spectral range. The proposed model is also versatile and can be easily extended to more complex configurations of TiN samples, including advanced structures like nanoantennas and metasurfaces. Additionally, we also show, for the first time to the best of our knowledge, that the tunability induced by variations in the fabrication parameters does not only concern the optical properties in the static regime, but it is found also in the ultrafast timescale. These results provide with a powerful tool to make a quantitative prediction on the broadband modulation of the dielectric properties of TiN-based nanomaterials in the ultrafast timescale.

2. Results

We aim at providing a detailed description of ultrafast physical processes in plasmonic TiN films. To this scope, we first develop an analytical model for the dynamical energy relaxation mechanisms in the TiN medium following excitation with fs-laser pulses, and subsequent variation of the permittivity. Then, we numerically solve the equations and, as a last step, we compare the theoretical results with experimental data acquired to this purpose. This approach, combining quantitative modelling with ultrafast broadband experiments, enables us to clearly disclose the photo-physical mechanisms of TiN ultrafast response. The system considered in our model is a 200 nm-thick TiN film supported by a soda lime glass substrate (sketch in **Figure 1a**). The corresponding sample has been fabricated by pulsed laser deposition (PLD) in high vacuum (the lowest pressure being 4×10^{-3} Pa), so as to obtain high compactness and an overall smooth surface. The film structure is nanocrystalline and the scanning electron microscopy (SEM) of the film (on silicon, in **Figure 1b**), shows a compact morphology characterized by a columnar-like growth. The static optical response of the film is experimentally characterized in terms of absorption and reflectivity spectra, shown in **Figure 1c** (solid lines). A broad absorption peak is present, centered in the ultraviolet (UV)–vis range (at ≈ 330 nm). Since the film has an essentially metallic behavior and the transmission approaches zero in the whole spectral range, the static reflectivity has a complementary behavior to absorption, thus exhibiting a dip at ≈ 330 nm. We calculate the static response of the film according to the transfer matrix method (TMM) for normal incidence,^[52] as reported in Section S1 (Supporting Information), and our simulations (**Figure 1c**, dashed lines) match well the two measured spectra. The optical parameters of TiN used in the calculation are the ones obtained by fitting the experimental data from spectroscopic ellipsometry. Through this experimental technique, we extract both the real (ϵ_1 , **Figure 1d**) and the imaginary (ϵ_2 , **Figure 1e**) components of the static dielectric permittivity of TiN. The experimental data (solid lines) are fitted using a Drude and one-Lorentz oscillator model, which provides a very good agreement with the measurements (compare dashed and solid lines). The fitting parameters can be found in

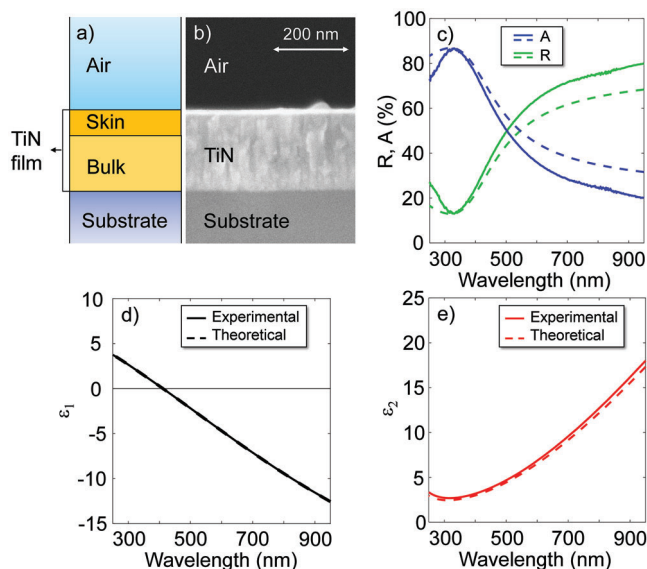


Figure 1. a) Sketch of the TiN film sample. b) Cross sectional SEM image of the TiN film (thickness 200 nm). c) Static optical response of the TiN film: absorption, A (blue curves) and reflectivity, R (green curves). Both experimental (solid curves) and theoretical (dashed curves) data are reported. d) Real, ϵ_1 and e) imaginary, ϵ_2 part of the dielectric permittivity of the TiN film: experimental (solid) and theoretical (dashed) curves.

Section S2 (Supporting Information). Note that our sample has a strong metallic character in the vis–NIR range, marked by the negative sign of ϵ_1 , while it exhibits a dielectric behavior in the UV, spectral region where ϵ_1 is positive. These characteristics are in accordance with literature.^[21,33] The crossover plasma wavelength λ_p , where the real part of the permittivity crosses zero, falls in the visible ($\lambda_p \approx 410$ nm). This value is typical of nitrogen-deficient TiN films,^[53] and in agreement with our deposition conditions (see Section S3, Supporting Information). The fitting of the experimental static optical functions is crucial when studying TiN samples, due to the high sensitivity of the dielectric permittivity to the specific synthesis conditions.^[21]

To characterise the ultrafast optical response of the TiN film, we need, first of all, a model able to describe the energy relaxation mechanisms following photoexcitation. This can be done by detailing the dynamics of the internal energy degrees of freedom of our system, namely the carrier and the lattice temperatures. For this purpose, we exploit the inhomogeneous 2TM.^[54,55] This is a thermodynamical model derived from the Boltzmann transport equation and describing the dynamics of photoexcitation as that of the heat exchange between two coupled reservoirs, both at thermal equilibrium. In our system, these are the hot electron population (carriers) at temperature T_C , photogenerated by the pump pulse (the latter being accounted for by the absorbed electromagnetic power density P_A , see Section S4, Supporting Information) and the TiN lattice, at temperature T_L . The applicability of the 2TM relies on two strong approximations: i) the instantaneous thermalization of the hot electron gas, so as to fill the material bands according to a Fermi–Dirac statistics throughout the entire dynamics, and ii) the internal thermal equilibrium of the phonon population. Therefore, this approach is limited to processes where it is possible to neglect the very ini-

tial stages of the ultrafast optical dynamics (indeed marked by a strong non-equilibrium electron population), electron–electron scattering, and anisotropic electron–hole excitation.^[56] TiN satisfies the requirements, exhibiting an electron–electron scattering taking place on few tens of fs timescale.^[44]

In our study, the pump wavelength and fluence are set to 500 nm and $160 \mu\text{J cm}^{-2}$, respectively, and the pump pulse temporal duration is fixed at 100 fs. The pump power is mostly absorbed in a thin layer at the top the TiN film. The thickness of this layer was estimated as the distance upon which most of the power (80%) is evanescently extinguished. This corresponds to a top layer of thickness $d_0 \approx 1.5d_{\text{skin}}$ with d_{skin} the optical skin depth $d_{\text{skin}} = \lambda_{\text{pump}} / (4\pi \text{Im}\{n\}) \approx 20$ nm, where n is the complex-valued refractive index at pump wavelength and Im stands for its imaginary part. Moreover, the model accounts for electron and phonon diffusion along a z -direction (perpendicular to the film thickness) as a result of an excitation provided by a space- and time- dependent source term. Any space-dependence along other directions can indeed be neglected, since the pump spot size (hundreds of μm in diameter) is much bigger than d_0 . The process can be quantitatively described by the following set of coupled rate-equations:

$$C_C \frac{\partial T_C}{\partial t} = -\nabla \cdot (-\kappa_C \nabla T_C) - G(T_C - T_L) + P_A(z, t) \quad (1)$$

$$C_L \frac{\partial T_L}{\partial t} = G(T_C - T_L) + \kappa_L \nabla^2 T_L \quad (2)$$

where $C_C = \gamma T_C$ is the electron gas heat capacity, γ being a constant, C_L is the heat capacity of the lattice, G is the electron–phonon coupling constant, κ_C and κ_L are, respectively, the thermal conductivities of electrons and lattice. TiN is marked by a prominent plasmonic character with an efficient carrier heating, embedded in $\gamma = 112.5 \text{ J m}^{-3} \text{ K}^{-2}$,^[43] which is twice the value in gold.^[48] Likewise, $G = 10^{18} \text{ W m}^{-3} \text{ K}^{-1}$ ^[43] exceeds that of gold ($G_{\text{Au}} = 2.5 \times 10^{16} \text{ W m}^{-3} \text{ K}^{-1}$) and silver ($G_{\text{Ag}} = 3 \times 10^{16} \text{ W m}^{-3} \text{ K}^{-1}$) by 2 orders of magnitude,^[57] denoting a very high electron–phonon coupling. These properties make it a very interesting material for ultrafast plasmonics. The lattice parameters are $C_L = 3.149 \times 10^6 \text{ J m}^{-3} \text{ K}^{-1}$ and $\kappa_L = 29 \text{ W m}^{-1} \text{ K}^{-1}$ ^[58,59] and the electronic thermal conductivity can be approximated^[60] to $k_C = k_L T_C / T_L$. The electronic population located in the optical skin heats up, and, in some tens of fs, exchanges energy with the phonon bath. Being the temporal scale for hot electron relaxation much faster than that of thermal diffusion (some ps), the hot electron population is expected not to reach the bulk layer before scattering with phonons. To rationalize the dominant contributions in the system dynamics, we first solve the inhomogeneous 2TM along the whole film thickness, obtaining two temperature profiles along the spatial coordinate z , namely $T_C(z)$ and $T_L(z)$. Subsequently, we extract four effective temperatures: two carrier and two lattice temperatures, defined separately, either within the skin layer or within the rest of the film (referred to as bulk layer hereafter). Specifically, T_C and T_L in the skin/bulk layer are calculated as the mean of their spatial profile in the layer of interest. In this way, we can reduce a spatially inhomogeneous system into two separate, homogeneous sub-systems. This simplification is extremely useful, since it enables us to determine the transient reflectivity via TMM, that is, in the same way as for the

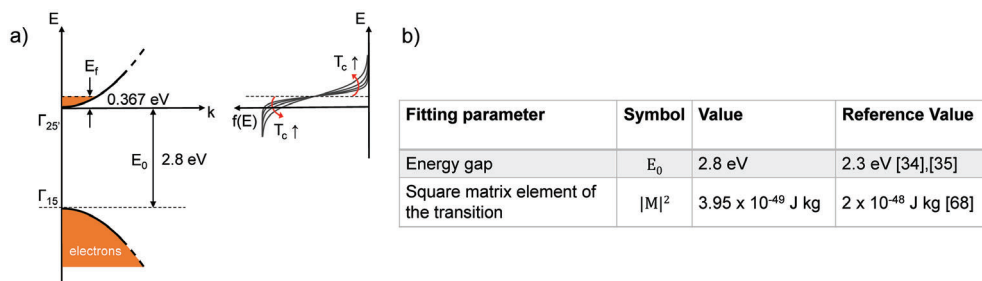


Figure 2. a) Sketch of the parabolic, isotropic bands assumed to be dominant in the transient optical response of TiN: we consider only one interband transition ($\Gamma_{15} \rightarrow \Gamma_{25'}$, 2.8 eV, 442 nm^[34,35]). The Fermi smearing, responsible for the interband transition modulation, is also shown. b) Table of fitting parameters for the model.

calculation of the static optical response, hence without resorting to more complex continuous differential models. Once these four temperature dynamics are numerically determined, the following modelling step consists in calculating the corresponding variation of the material's dielectric permittivity $\Delta\epsilon$, in each layer. Notably, $\Delta\epsilon$ is made up of two contributions: one related to the interband transitions $\Delta\epsilon_{IB}$ and one concerning instead the intraband transitions (Drude–Sommerfeld contribution) $\Delta\epsilon_{DS}$.

The modulation of interband transitions depends on how the electronic Fermi distribution f_0 at room temperature (T_0) is perturbed under the effect of the pump pulse. In particular, as a result of the carrier temperature increase ($T_C > T_0$), the occupation probability of the electron states below (above) the Fermi energy is reduced (increased), leading to a decreased (increased) interband absorption for transitions involving final states above (below) the Fermi level.^[61] This mechanism, commonly referred to as *Fermi smearing* (Figure 2), corresponds to a modulation of the Fermi–Dirac occupancy distribution given by:

$$\Delta f(E, t) = f_0[E, T_C(t)] - f_0[E, T_0], \quad (3)$$

where E is the electron energy measured from the Fermi level. We consider only thermalized electrons, neglecting the contributions from the very initial non-thermal population, coupled to the thermalized one via electron–electron scattering interactions, consistently with the assumptions of the 2TM.

Figure 2a displays a simplified scheme for TiN band structure.^[34,35] Several parameters are needed to solve the calculations in our model. Some of them are taken from literature, others are kept as fitting constants of our experimental pump-probe data. The latter are obtained by rescaling the values found in previous works, while maintaining a good agreement with the reference values. A few parameters, not reported in literature, are simply re-scaled from what found in gold. The fitting parameters are reported in the table of Figure 2b. Few approximations are needed to retrieve $\Delta\epsilon_{IB}$. We consider TiN bands to be parabolic and isotropic, and one interband transition only to be relevant in the transient regime: $\Gamma_{15} \rightarrow \Gamma_{25'}$. This is the only case in which the states in the arrival level (the Fermi level, $E_F = 0.367$ eV measured from the bottom of the conduction band^[34]) are occupied at T_0 , so it will be the most affected transition by Fermi smearing, following pump excitation. Indeed, the mechanism governing the transient response is the transitions' modulation, and not the bare presence of transitions as for the static regime. The

value here employed for E_f should not be confused with the one retrieved by a simplified free-electron model, from the free carrier density (see Section S5, Supporting Information). The energy gap, E_0 , is a fitting parameter for our model, and turned out to be $E_0 = 2.8$ eV, which is not far from the value reported in previous works,^[34,35] also considering the typical underestimation of about 1 eV retrieved by local density approximation in band structure calculations, as pointed out in Ref. [35]. The modification of the Fermi distribution Δf induces, in turn, a variation of the joint density of states (J_{DOS}) involved in the specific transition, and with this, we can write the modulation of the imaginary part of the interband permittivity $\Delta\epsilon''_{IB}(\lambda, t)$ (in the constant matrix element approximation, λ being the probe wavelength) similarly to what reported for more conventional plasmonic metals such as, for example, silver^[61] (see Section 7 for details). The corresponding real part of the modulation of the interband dielectric function $\Delta\epsilon'_{IB}(\lambda, t)$ is then found from the Kramers–Kronig relations. For what concerns the modulation of the permittivity related to intraband transitions, it arises from two different phenomena. The first is the variation of the Drude damping factor Γ (Drude broadening). This variation is caused by an increment in the electron scattering rate with phonons:^[62]

$$\Delta\Gamma(\omega, t) = b(\hbar\omega)^2(T_L(t) - T_0). \quad (4)$$

In the last equation, $b = 2.143 \times 10^{48} (\text{J}^2\text{K s})^{-1}$ is the broadening coefficient for electron–phonon collisions, and it is set close to the value provided in Ref. [62] for gold.

The second phenomenon involved in the modulation of the Drude part of the permittivity is related to the variation of the plasma frequency, ω_p , following photoexcitation. For our system, over the volume increase due to thermal expansion, we need to take into account also the generation of an elastic stress in the sample, induced by the interaction with the pump pulse, to correctly model the response. This stress, in turn, sets up acoustic waves in the film. To perform the calculations, we exploit the thermoelastic model from Ref. [63], where the sample absorbs an energy $W(z) = AF/d_0 e^{-z/d_0}$ and the temperature increases by $\Delta T(z) = W(z)/C_L$, where A is the sample absorption and F is the pump fluence. We suppose this temperature driving term to be time-independent, since the temporal scale for the acoustic wave generation falls in a range in which the lattice temperature is approximately constant over time. The phenomenon can be

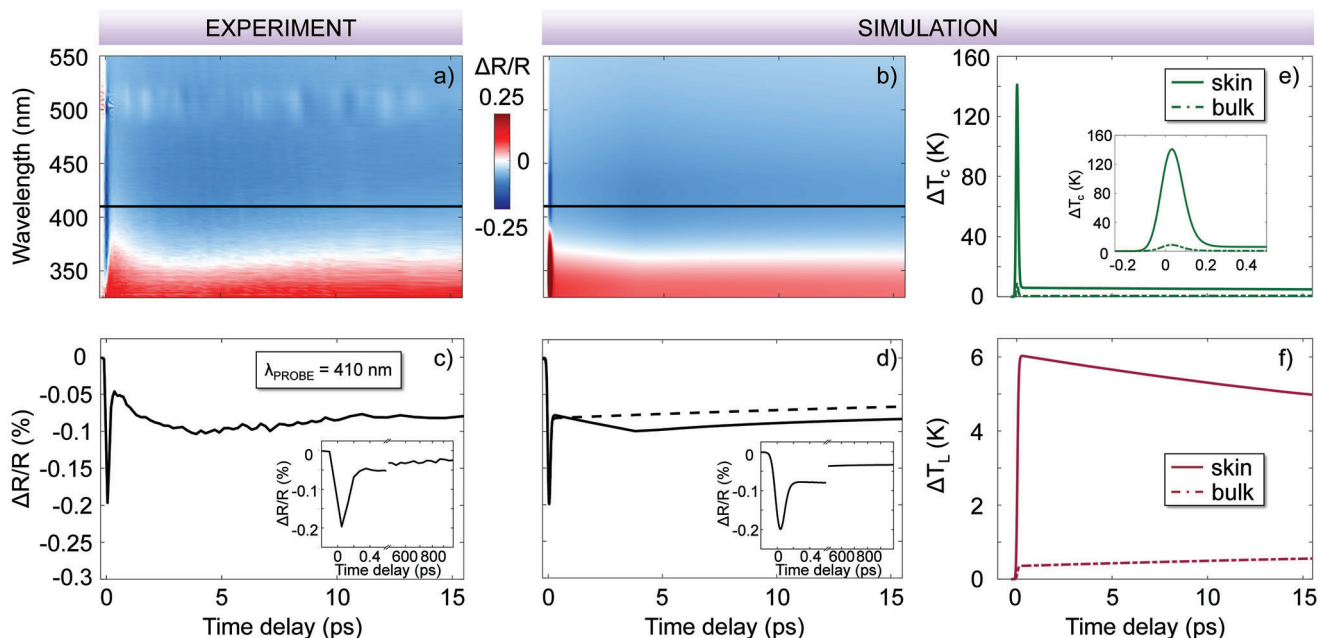


Figure 3. a) Experimental and b) numerical pump-probe map of the TiN film on glass. Pump wavelength: 500 nm; incident fluence: $130 \mu\text{J cm}^{-2}$ (experimental); $160 \mu\text{J cm}^{-2}$ (theoretical); pump pulse temporal duration: 100 fs. c) Experimental and d) theoretical pump-probe signal dynamics at 410 nm with (solid curve) and without (dashed curve) thermoelastic effects. Insets: dynamics zoom up to 600 fs and after 500 ps. e, f) Numerical model of the temporal dynamics of (e) electron and (f) lattice temperatures in skin and bulk layers (solid and dashed lines, respectively).

properly described by the D'Alembert equation for the displacement u along z -direction, with the temperature as driving term:

$$\frac{\partial^2 u(z, t)}{\partial t^2} = v^2 \frac{\partial^2 u(z, t)}{\partial z^2} + \beta \frac{\partial T(z)}{\partial z} \quad (5)$$

where $\beta = -3Y\alpha_L/\rho$ is a constant, containing the Young modulus $Y = 300 \text{ GPa}$ (highest value in the temperature range considered in [64]), the linear expansion coefficient $\alpha_L = 8.3 \times 10^{-6} \text{ K}^{-1}$ and the density $\rho = 5.21 \times 10^3 \text{ kg m}^{-3}$ of TiN.^[65,66] By solving the above equation, the deformation $\eta(z, t)$ along the z -direction is retrieved at each temporal delay (see Section 7 for details), and then the skin layer thickness variation can be determined as $\Delta d_0(t) = \int_0^{d_0} \eta(z, t) dz$. This modulation is in turn responsible for a plasma frequency modulation in the skin layer, which can be computed as:

$$\Delta \omega_p(t) = -\frac{1}{2} \frac{\omega_p}{d_0} \Delta d_0(t). \quad (6)$$

The acoustic strain waves are dominant in the skin layer and rapidly decay with an exponential trend. Similarly to the case of gold, we neglect other contributions to the variation of ω_p due to, for example, the increase in the number of carriers in the conduction band. As a result, the plasma frequency modulation in the bulk layer is much lower and solely due to adiabatic thermal expansion. The permittivity modulations arising from the Drude damping increase, $\Delta \epsilon_{DS,\Gamma}(\omega, t)$, and from the plasma frequency variation, $\Delta \epsilon_{DS,\omega_p}(\omega, t)$, can be straightforwardly calculated according to the Drude model of noble metal permittivity, as detailed in Section 7, Equations 10 and 11). Finally,

the total variation of the Drude part of the dielectric function is $\Delta \epsilon_{DS}(\omega, t) = \Delta \epsilon_{DS,\Gamma}(\omega, t) + \Delta \epsilon_{DS,\omega_p}(\omega, t)$, while the overall permittivity modulation becomes:

$$\Delta \epsilon = \Delta \epsilon_{IB} + \Delta \epsilon_{DS}. \quad (7)$$

Subsequently, exploiting iteratively over time the TMM, we calculate how the optical properties vary as a result of the excitation induced by the laser pump pulse.

3. Model Validation

We compare the results of the numerical model to experimental data obtained by ultrafast pump-probe transient reflection spectroscopy. The pump wavelength and fluence are set in accordance to the simulation at 500 nm (2.48 eV) and $\approx 130 \mu\text{J cm}^{-2}$, respectively. The pump wavelength is tuned far enough from the plasma frequency of our sample, to monitor this spectral region.

The comparison between experimental and numerical results is shown in **Figure 3a,b**. Our model is able to reproduce the experiment with a high degree of accuracy on a broad wavelength range, both in the sub-ps range and at longer temporal delays. The TiN film ultrafast optical response shows two lobes of opposite sign: a positive one for wavelengths below $\approx 370 \text{ nm}$ and a negative one at longer wavelengths. Looking deeply at the differential reflectivity signal dynamics, shown in **Figure 3c,d** for an exemplary probe wavelength of $\lambda_{\text{PROBE}} = 410 \text{ nm}$, we notice an ultrafast (negative) peak extinguishing in about 200 fs, followed by a slower signal rise which takes $\approx 4.5 \text{ ps}$ to reach a secondary and smoother (negative) peak, before decreasing again on a longer time scale. To accurately resolve the ultrafast peak, we perform a

further measurement with a temporal resolution of ≈ 18 fs (reported in Section S6, Supporting Information). We find that the signal rise and decay take place in ≈ 50 and ≈ 80 fs. The peak is thus rationalised in terms of the excitation and subsequent relaxation of hot electrons. Indeed, literature^[44] suggests that the ultrafast signal rise is due to the heating of the carrier population via electron-electron scattering interactions. This phenomenon is assumed instantaneous in our model, thus the generation of the thermalized hot electron population follows the pump pulse absorption. On the other hand, the signal decay is dictated by the intrinsic dynamical response of the system. The model proves the signal decay to be ascribed to hot electron relaxation through electron-phonon scattering. According to the 2TM of Equations 1 and 2, the decay rate of the hot electron temperature in the skin layer can be estimated as $G/\gamma T_0$ (with T_0 the room temperature), corresponding to a time constant $\tau_E = \gamma T_0/G \approx 34$ fs, when taking the same values of parameters used in our simulations, in accord with the signal peak decay time measured in our pump-probe experiments. For what concerns the slower signal rise after the first peak, it cannot be caused by simple phonon-phonon interactions. The result of this phenomenon would be, indeed, a progressive monotonic reduction of the differential reflection, since the energy provided by the pump pulse would be dissipated into the external environment. We prove, instead, that only including the thermoelastic processes into our numerical model, it is possible to accurately reproduce the slow rise. For a clearcut evaluation of the contribution provided by this phenomenon, in Figure 3d we also show a simulated temporal trace for a simplified model neglecting the thermoelastic processes (dashed curve): note that the rebirth of the signal with the secondary peak observed at around 4.5 ps is completely missing. Contrarily to previous reports,^[43,44] our numerical model allows predicting the variation of the optical properties of the TiN film on a broad spectral domain, not confining the analysis to the single-wavelength dynamics. This goal is reached by the complete formulation of the permittivity modulation induced by the pump pulse proposed in this work.

4. Discussion

We can thus consider our model validated and derive the temperature profiles from the 2TM (Figure 3e,f). The electron population rises its temperature and cools down until almost reaching room temperature in about 200 fs (see inset of Figure 3e). This is expressed by the ultrafast dynamics of the peak in Figure 3e, whose decay represents the cooling due to electron-phonon interaction.

A further slow decay of T_L , due to the heat diffusion in the TiN film, takes place, then, in more than 1 ns (see Section S7, Supporting Information). Lattice heating starts concurrently to the energy release from the hot electrons to the phonon population, and the lattice temperature temporal behavior is remarkably different from the electronic one. In this case, the temperature decay is much slower, so that ΔT_L can be considered approximately constant on a temporal scale of a few tens of ps. However, following the rapid transient during which the heat exchange between electron and phonon baths takes place, a uniform temperature is reached in both layers ($T_C = T_L$). We note that temperature variations can be considered relevant only in the optical skin layer, where ΔT_C reaches ≈ 140 K and $\Delta T_L \approx 6$ K. These results suggest

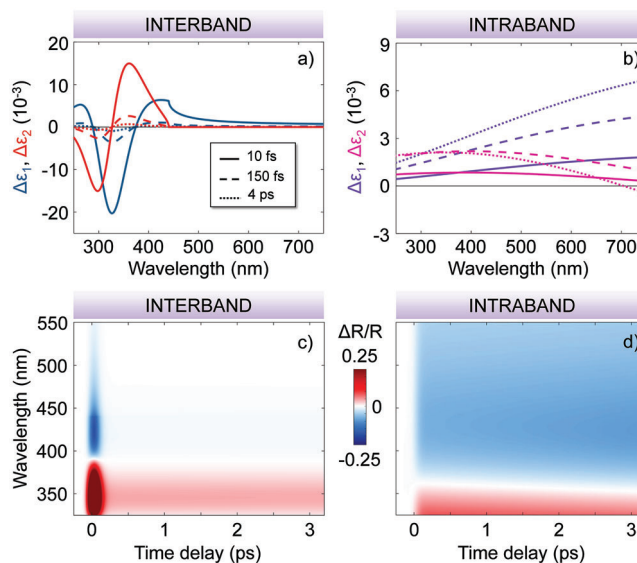


Figure 4. a,b) Real (blue/purple curves) and Imaginary (red/pink curves) part of the modulation of dielectric properties of TiN in the optical skin layer due to (a) carriers and (b) lattice contribution at different time delays following pump excitation: $t = 10$ fs (solid line), $t = 150$ fs (dashed line), $t = 4$ ps (dotted line). c,d) Pump-probe theoretical map of the TiN film showing the disentanglement of (c) interband and (d) lattice contributions to the modulation of $\Delta\epsilon$.

the relevance of the skin layer in this system, together with the accuracy of our approach in taking it into account for the description of the ultrafast optical properties of TiN.

The numerical model above described also enables us to disentangle the two different contributions of the permittivity modulation to the transient optical signal (Equation 11). This is of crucial importance, since, for the first time, we could quantify each modulation of $\Delta\epsilon$ on the whole spectral range of interest and determine its timescale. In Figure 4a,b, we show the spectral variation of the interband and intraband permittivity, respectively, at 10 fs (solid line), 150 fs (dashed line), and 4 ps (dotted line) temporal delay after photoexcitation. Thanks to such disentanglement, it is possible to notice that the maximum of the interband modulation (on the whole spectrum) at the peak of the ultrafast signal (≈ 10 fs) is one order of magnitude higher than the intraband modulation evaluated at the same time delay (compare solid lines in Figure 4a,b). This difference evolves over time and it becomes negligible for temporal delays of ≈ 150 fs. Moreover, we can also observe that the two contributions have remarkably different spectral features, in the range of interest. Indeed, the interband part peaks at transitions having an energy $E \approx E_0 + E_F$ (≈ 3.17 eV), since below (above) the Fermi level the pump pulse is responsible for the creation of free (occupied) electronic states. Therefore, these transitions are the most affected during the transient regime. Far from $E_0 + E_F$, at lower energies, the interband modulation is much weaker and dominated by its real part. Both real and imaginary parts of $\Delta\epsilon_{IB}$ are stronger in the earliest stages of the dynamics, right after pump excitation, and they become negligible already after a few ps. Conversely, the intraband part is less dispersed in the probe spectrum, and increases faster at longer wavelengths. Observing $\Delta\epsilon_{DS}$ evolution over time, it is possible to notice that

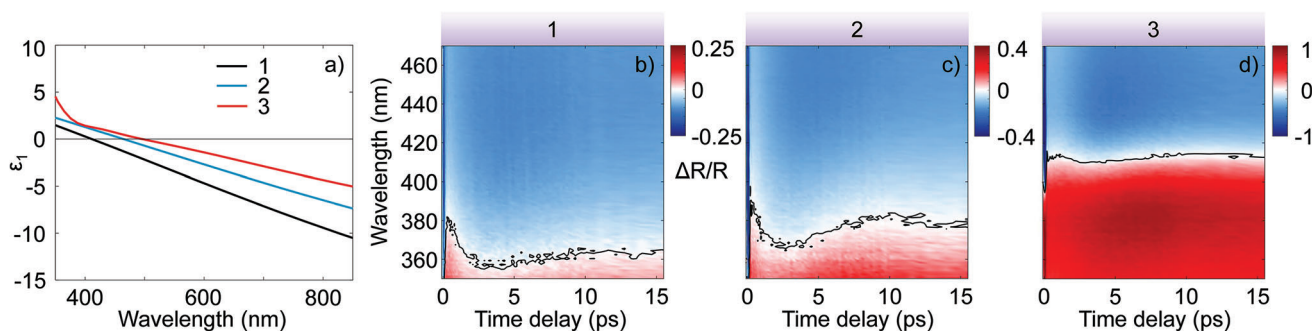


Figure 5. a) Static dielectric permittivity (real part) of three different TiN films on glass (Samples 1–3) fabricated by PLD, in different conditions. Sample 1 (black curve): $\lambda_{p1} = 410$ nm. Sample 2 (blue curve): $\lambda_{p2} = 460$ nm. Sample 3 (red curve): $\lambda_{p3} = 500$ nm. Data obtained through spectroscopic ellipsometry measurements. b–d) Pump-probe experimental map (respectively) of Samples 1–3. We can observe the isosbestic line red shifts from Sample 1 to 3 accordingly to λ_p .

the real part increases monotonically, similarly to what happens in gold,^[67] while this does not occur for the imaginary part. This can be attributed to the different value for Γ , which is almost one order of magnitude lower compared to the one of gold.^[67]

Furthermore, in Figure 4c we show the simulated map of the ultrafast differential reflectivity signal $\Delta R/R$, where only the variation of the interband permittivity is present. In Figure 4d, on the contrary, only the modulation of the dielectric function due to intraband transitions is shown. Consistently with the $\Delta\epsilon$ spectra of Figure 4a,b, also from the transient maps of differential reflectivity (Figure 4c,d) we notice that the Drude part becomes relevant at longer time delays ($t > \approx 200$ fs) with respect to the interband one. Our model enables to show that the interband transitions modulation is crucial in the ultrafast optical response of TiN. Neglecting its contribution prevents indeed from capturing the ultrafast features of this material. On the other hand, these results reinforce our previous approximation in considering the film thermal expansion as the only responsible for the plasma frequency modulation. Indeed, we suppose carrier relaxation to take place on a much lower timescale (tens of fs) than the Drude modulation. As previously mentioned, TiN boasts the possibility of tuning its static optical properties by varying the synthesis conditions.^[53] As a completion of this work, we demonstrate that this tuning is not limited to the static reflection spectra, as it couples to a change in the transient optical response as well.

To show this interesting behavior, we display in **Figure 5** the ultrafast pump-probe experimental data on three TiN films on glass, having the same thickness $d = 200$ nm but fabricated by PLD in different conditions, in terms of deposition atmosphere and post-deposition annealing treatments (see Section S8, Supporting Information). Sample 1 is the TiN film measured and studied for our model's validation (see previous sections). We can see that the permittivity curve (real part) is shifted moving from Sample 1 to 3. The crossover plasma wavelengths are $\lambda_{p1} = 410$, $\lambda_{p2} = 460$, and $\lambda_{p3} = 500$ nm, for Samples 1–3, respectively. Interestingly, we can notice from the pump-probe experimental maps (Figure 5b–d), that the isosbestic line is tuned accordingly, from Sample 1 to 3. This is particularly promising, since we can set the experimental fabrication conditions in such a way to engineer a TiN-based photonic device. For example, it is possible to enhance the ultrafast nonlinear response of a specific wavelength/spectral range.

5. Conclusion

In conclusion, we formulated a numerical model for the optical nonlinearity of TiN, combining a thermodynamic description of the ultrafast dynamics of nonequilibrium electronic and phononic states in the material (by means of a Two-Temperature Model, 2TM) and the semiclassical modelling of optical nonlinearities at the nanoscale. The model provides a quantitative prediction of how the dielectric properties of the material change after ultrafast photoexcitation, not only in time (i.e., for a single wavelength) but also on a broad spectral domain. Indeed, we were able, for the first time to the best of our knowledge, to disentangle the interband and intraband contributions to the modulation of the permittivity, and thus explain the origin of the giant ultrafast optical response of TiN-based materials upon irradiation with intense fs-laser pulses. The maximum (in time and in the analyzed spectral range) of the interband part is one order of magnitude higher than the intraband part, and, after ≈ 150 fs following pump excitation, the two become comparable. For long temporal delays (picoseconds) the Drude contribution dominates the material's optical dynamics. Finally, we proved that changing the fabrication conditions can imprint a tuning not only in the static optical response of TiN films, but in the transient one as well. These findings are crucial both to set a complete physical insight of the material's properties in general, and when considering TiN as a novel material for ultrafast plasmonics, in view of device design. Compared to conventional plasmonic materials, the ultrafast modulation photoinduced in TiN is intriguing, as a consequence of the high electron gas heating and of its strong electron-phonon interactions with respect to traditional plasmonic materials such as, for example, gold. This work opens up new interesting developments, such as the application of the model to other TiN structures such as nanoantennas, or to even more complex layouts like metasurfaces, in view of the exploitation of this material into new, faster devices performing, for example, all optical modulation of light.

6. Experimental Section

Sample Preparation and Static Optical Characterization: The titanium nitride (TiN) film was produced via pulsed laser deposition from a high

purity (99.9% Mateck GmbH) TiN target. The ablation was performed exploiting a nanosecond pulsed laser (second harmonic of Nd:YAG, $\lambda = 532$ nm), with pulse duration of ≈ 6 ns and 10 Hz repetition rate. The laser fluence was set to 1.7 J cm^{-2} . The sample was placed at a distance of 50 mm in front of the target, mounted on a rotating sample holder. The process occurs in vacuum (4×10^{-3} Pa), for 2 h. The deposition takes place on a soda lime glass substrate, which was previously cleaned with isopropanol in an ultrasonic bath. In order to evaluate the homogeneity of the surface of the deposited film, the same TiN film was analyzed on a silicon substrate with a field emission scanning electron microscope (SEM, Zeiss SUPRA 40). Measurements of static reflectance and transmittance were performed with a Perkin Elmer Lambda 1050 spectrophotometer having a 150 mm diameter Spectralon-coated integrating sphere ($R > 95\%$ in the range of 250–2000 nm, $R > 99\%$ in the range of 400–1500 nm). The sample absorbance was then simply calculated as $A = 1 - T - R$. Transmission measurements were performed at normal incidence, while reflectance data were collected with the sample tilted by an angle of 8° to enable the detection of the specular component. The spectroscopic ellipsometry measurements were performed with a J. A. Woollam NIR–UV variable-angle spectroscopic ellipsometer (V-VASE) in the range of 0.6–6.5 eV with the energy interval of 0.1 eV at two angles of incidence (65° and 75°). The analysis and modelling of the ellipsometric spectra were performed by the WVASE32 (J. A. Woollam Co.) software.

Transient Reflectivity Measurements: The pump-probe setup was based on an amplified Ti:sapphire laser delivering pulses at 2 kHz repetition rate, central wavelength at 800 nm and temporal duration of ≈ 100 fs. The pump beam was generated via noncollinear optical parametric amplification (NOPA), enabling a tunable beam in the visible and NIR range (490–770 nm). The delayed probe beam was a white light supercontinuum generated by focusing the fundamental 800-nm pulse into a 3-mm thick CaF_2 plate (range 310–600 nm). The probe reflection from the film was collected by a computer-controlled multichannel analyzer. The delay among pump and probe was electronically controlled through a translation stage. The measurement result was a differential signal $[R_{ON}(\lambda_{PROBE}, \tau) - R_{OFF}(\lambda_{PROBE})]/R_{OFF}(\lambda_{PROBE}) = \Delta R/R$ as function of probe wavelength λ_{PROBE} and pump-probe delay τ , giving rise to a bidimensional map. R_{ON} was the reflected spectrum from the excited sample, while R_{OFF} was the one as recorded in absence of the pump pulse.

Model Equations: The JDOS was computed according to the parabolic band approximation:

$$\Delta J_{DOS}(\lambda, t) = -\frac{2}{4\pi^2} \left(\frac{2m_r}{\hbar^2} \right)^{3/2} \sqrt{\frac{\hbar c}{\lambda} - E_0} \Delta f(E_\lambda, t) \quad (8)$$

In the equation above, $m_r = m_e m_h / (m_e + m_h)$ was the system's effective reduced mass, with $m_e = 1.2m_0$ and $m_h = 0.72m_0$ the electron and hole effective mass in the conduction and valence bands, respectively (with m_0 the free electron mass). Their values were fitted on the calculated band structure of TiN reported in Ref. [34], while $E_\lambda = m_r/m_e (\hbar c/\lambda - E_0) - E_F$. The other reported quantities were the Planck's constant \hbar , the probe wavelength λ , and the light speed in vacuum c . With this, the modulation of the imaginary part of the interband permittivity was written (in the constant matrix element approximation) as follows, similarly to what reported for more conventional plasmonic metals such, for example, silver:^[61]

$$\Delta \epsilon''_{IB}(\lambda, t) = \frac{1}{12\pi\epsilon_0} \left(\frac{e\lambda}{m_0 c} \right)^2 |M|^2 \Delta J_{DOS}(\lambda, t) \quad (9)$$

Here, $|M|^2$ was the square of the constant matrix element of the considered transition, whose value was fitted on the experimental data, and resulted to be $|M|^2 = 3.95 \times 10^{-49} \text{ J kg}$. This value was rescaled from the one used for gold in Ref. [68].

The variation of permittivity due to the Drude broadening was:

$$\Delta \epsilon_{DS,\Gamma}(\omega, t) = \frac{i\omega_p^2 \Delta\Gamma(\omega, t)}{\omega(\omega + i\Gamma)[\omega + i\Gamma + i\Delta\Gamma(\omega, t)]} \quad (10)$$

where ω_p is the plasma frequency.

Both for the skin and bulk layer, the modulation of the Drude permittivity due to ω_p decrease can be computed as:

$$\Delta \epsilon_{DS,\omega_p}(\omega, t) = -\frac{\Delta\omega_p(t)[\Delta\omega_p(t) + 2\omega_p]}{\omega(\omega + i\Gamma)} \quad (11)$$

The solution to D'Alembert Equation 5 was given by:

$$\eta(z, t) = \frac{\partial u(z, t)}{\partial z} = \frac{AF\alpha_L}{d_0 C_L} \frac{1 + \nu}{1 - \nu} F(z - \nu t) \quad (12)$$

Here, $\nu = 0.5$ was the Poisson's ratio, in line with the range of values reported in Ref. [69] for TiN, and $F(z - \nu t) = e^{-z/d_0} (1 - \frac{1}{2} e^{-\nu t/d_0}) - \frac{1}{2} e^{-|z-\nu t|/d_0} \text{sgn}(z - \nu t)$,^[63] with sgn the sign function.

Supporting Information

Supporting Information is available from the Wiley Online Library or from the author.

Acknowledgements

G.D.V. and M.Z.-R. contributed equally to this work. This publication was part of the METAFast project that received funding from the European Union Horizon 2020 Research and Innovation programme under grant agreement no. 899673. This work reflects only author view and the European Commission was not responsible for any use that may be made of the information it contains. A.L.B. acknowledges funding by: • Funder: Project funded under the National Recovery and Resilience Plan (NRRP), Mission 4 Component 2 Investment 1.3 - Call for tender no. 1561 of 11.10.2022 of Ministero dell'Università e della Ricerca (MUR); funded by the European Union - NextGenerationEU. • Award Number: Project code PE0000021, Concession Decree No. 1561 of 11.10.2022 adopted by Ministero dell'Università e della Ricerca (MUR), CUP D43C22003090001, Project title "Network 4 Energy Sustainable Transition - NEST". L.M. and A.N. acknowledge the support from the Czech Science Foundation (GACR) through the project 22-26416S and from the Ministry of Education, Youth and Sports of the Czech Republic (MEYS CR) through the CzechNanoLab project LM2018110 for the ellipsometry measurements at CEITEC Nano Research Infrastructure. A.N. acknowledges the support from the Project CH4.0 under the MIUR program "Dipartimenti di Eccellenza 2023-2027" (CUP: D13C2200352001).

Open Access Funding provided by Politecnico di Milano within the CRUI-CARE Agreement.

Conflict of Interest

The authors declare no conflict of interest.

Data Availability Statement

The data that support the findings of this study are available from the corresponding author upon reasonable request.

Keywords

hot electrons, plasmonic materials, titanium nitride, ultrafast transient absorption spectroscopy, ultrafast plasmonics

Received: February 10, 2023

Revised: March 21, 2023

Published online: May 5, 2023

- [1] S. A. Maier, M. L. Brongersma, P. G. Kik, S. Meltzer, A. A. Requicha, H. A. Atwater, *Adv. Mater.* **2001**, *13*, 1501.
- [2] J. A. Schuller, E. S. Barnard, W. Cai, Y. C. Jun, J. S. White, M. L. Brongersma, *Nat. Mater.* **2010**, *9*, 193.
- [3] W. A. Murray, W. L. Barnes, *Adv. Mater.* **2007**, *19*, 3771.
- [4] P. K. Jain, X. Huang, I. H. El-Sayed, M. A. El-Sayed, *Acc. Chem. Res.* **2008**, *41*, 1578.
- [5] K. A. Willets, R. P. Van Duyne, *Annu. Rev. Phys. Chem.* **2007**, *58*, 267.
- [6] T. J. Davis, D. E. Gómez, A. Roberts, *Nanophotonics* **2016**, *6*, 543.
- [7] E. Cortés, F. J. Wendisch, L. Sortino, A. Mancini, S. Ezendam, S. Saris, L. de S. Menezes, A. Tittl, H. Ren, S. A. Maier, *Chem. Rev.* **2022**, *122*, 15082.
- [8] A. Naldoni, V. M. Shalae, M. L. Brongersma, *Science* **2017**, *356*, 908.
- [9] G. V. Hartland, L. V. Besteiro, P. Johns, A. O. Govorov, *ACS Energy Lett.* **2017**, *2*, 1641.
- [10] M. L. Brongersma, N. J. Halas, P. Nordlander, *Nat. Nanotechnol.* **2015**, *10*, 25.
- [11] K. F. MacDonald, Z. L. Sámsón, M. I. Stockman, N. I. Zheludev, *Nat. Photonics* **2009**, *3*, 55.
- [12] A. Boltasseva, H. A. Atwater, *Science* **2011**, *331*, 290.
- [13] A. Comin, L. Manna, *Chem. Soc. Rev.* **2014**, *43*, 3957.
- [14] G. V. Naik, V. M. Shalae, A. Boltasseva, *Adv. Mater.* **2013**, *25*, 3264.
- [15] I. Kriegel, F. Scotognella, L. Manna, *Phys. Rep.* **2017**, *674*, 1.
- [16] R. Gaspari, G. Della Valle, S. Ghosh, I. Kriegel, F. Scotognella, A. Cavalli, L. Manna, *Nano Lett.* **2017**, *17*, 7691.
- [17] U. Guler, G. V. Naik, A. Boltasseva, V. M. Shalae, A. V. Kildishev, *Appl. Phys. B* **2012**, *107*, 285.
- [18] G. V. Naik, J. Kim, A. Boltasseva, *Opt. Mater. Express* **2011**, *1*, 1090.
- [19] S. Yu, Q. Zeng, A. R. Oganov, G. Frapper, L. Zhang, *Phys. Chem. Chem. Phys.* **2015**, *17*, 11763.
- [20] J. Goscinia, F. B. Atar, B. Corbett, M. Rasras, *Sci. Rep.* **2019**, *9*, 1.
- [21] A. Kharitonov, S. Kharitintsev, *Opt. Mater. Express* **2020**, *10*, 513.
- [22] C. M. Zgrabik, E. L. Hu, *Opt. Mater. Express* **2015**, *5*, 2786.
- [23] W. Li, U. Guler, N. Kinsey, G. V. Naik, A. Boltasseva, J. Guan, V. M. Shalae, A. V. Kildishev, *Adv. Mater.* **2014**, *26*, 7959.
- [24] S. Ishii, R. P. Sugavaneshwar, T. Nagao, *J. Phys. Chem. C* **2016**, *120*, 2343.
- [25] S. Molesky, C. J. Dewalt, Z. Jacob, *Opt. Express* **2013**, *21*, A96.
- [26] L. Mascaretti, A. Schirato, R. Zbořil, Š. Kment, P. Schmuki, A. Alabastri, A. Naldoni, *Nano Energy* **2021**, *83*, 105828.
- [27] S. H. Askes, E. C. Garnett, *Adv. Mater.* **2021**, *33*, 2105192.
- [28] A. Naldoni, Z. A. Kudyshev, L. Mascaretti, S. P. Sarmah, S. Rej, J. P. Froning, O. Tomanec, J. E. Yoo, D. Wang, S. Kment, T. Montini, P. Fornasiero, V. M. Shalae, P. Schmuki, A. Boltasseva, R. Zboril, *Nano Lett.* **2020**, *20*, 3663.
- [29] S. Saha, A. Dutta, N. Kinsey, A. V. Kildishev, V. M. Shalae, A. Boltasseva, *ACS Photonics* **2018**, *5*, 4423.
- [30] N. Sun, D. Zhou, W. Liu, A. Li, Y. Su, P. Jiang, Y. Zou, S. Shi, F. Liu, *J. Power Sources* **2021**, *489*, 229406.
- [31] X. Wen, G. Li, C. Gu, J. Zhao, S. Wang, C. Jiang, S. Palomba, C. Martijn de Sterke, Q. Xiong, *ACS Photonics* **2018**, *5*, 2087.
- [32] L. Gui, S. Bagheri, N. Strohhfeldt, M. Hentschel, C. M. Zgrabik, B. Metzger, H. Linnenbank, E. L. Hu, H. Giessen, *Nano Lett.* **2016**, *16*, 5708.
- [33] P. Patsalas, N. Kalfagiannis, S. Kassavetis, *Materials* **2015**, *8*, 3128.
- [34] V. Ern, A. Switendick, *Biophys. Rev.* **1965**, *137*, A1927.
- [35] P. Patsalas, S. Logothetidis, *J. Appl. Phys.* **2001**, *90*, 4725.
- [36] H. Reddy, U. Guler, Z. Kudyshev, A. V. Kildishev, V. M. Shalae, A. Boltasseva, *ACS Photonics* **2017**, *4*, 1413.
- [37] M. Kumar, S. Ishii, N. Urnezawa, T. Nagao, *Opt. Mater. Express* **2016**, *6*, 29.
- [38] S. Rej, E. Y. Santiago, O. Baturina, Y. Zhang, S. Burger, S. Kment, A. O. Govorov, A. Naldoni, *Nano Energy* **2022**, *104*, 107989.
- [39] A. Naldoni, U. Guler, Z. Wang, M. Marelli, F. Malara, X. Meng, L. V. Besteiro, A. O. Govorov, A. V. Kildishev, A. Boltasseva, V. M. Shalae, *Adv. Opt. Mater.* **2017**, *5*, 1601031.
- [40] T. Reese, A. N. Reed, A. D. Sample, F. Freire-Fernández, R. D. Schaller, A. M. Urbas, T. W. Odom, *ACS Photonics* **2021**, *8*, 1556.
- [41] H. Ferguson, U. Guler, N. Kinsey, V. Shalae, T. Norris, A. Boltasseva, in *CLEO: QELS_Fundamental Science*, Optica Publishing Group, San Jose, California, USA **2016**, pp. FF2D–1.
- [42] H. Ferguson, U. Guler, N. Kinsey, V. Shalae, T. Norris, A. Boltasseva, in *CLEO: Applications and Technology*, Optica Publishing Group, San Jose, California, USA **2017**, pp. JTh2A–22.
- [43] S. Dal Forno, J. Lischner, *Phys. Rev. Mater.* **2019**, *3*, 115203.
- [44] B. T. Diroll, S. Saha, V. M. Shalae, A. Boltasseva, R. D. Schaller, *Adv. Opt. Mater.* **2020**, *8*, 2000652.
- [45] A. Schirato, M. Maiuri, A. Toma, S. Fugattini, R. Proietti Zaccaria, P. Laporta, P. Nordlander, G. Cerullo, A. Alabastri, G. Della Valle, *Nat. Photonics* **2020**, *14*, 723.
- [46] G. Sartorello, N. Olivier, J. Zhang, W. Yue, D. J. Gosztola, G. P. Wiederrecht, G. Wurtz, A. V. Zayats, *ACS Photonics* **2016**, *3*, 1517.
- [47] M. R. Shcherbakov, S. Liu, V. V. Zubuyuk, A. Vaskin, P. P. Vabishchevich, G. Keeler, T. Pertsch, T. V. Dolgova, I. Staude, I. Brener, A. A. Fedyanin, *Nat. Commun.* **2017**, *8*, 1.
- [48] M. Zavelani-Rossi, D. Polli, S. Kochtcheev, A.-L. Baudrion, J. Béal, V. Kumar, E. Molotokaite, M. Marangoni, S. Longhi, G. Cerullo, P.-M. Adam, G. Della Valle, *ACS Photonics* **2015**, *2*, 521.
- [49] G. Della Valle, M. Conforti, S. Longhi, G. Cerullo, D. Brida, *Phys. Rev. B* **2012**, *86*, 155139.
- [50] X. Wang, Y. Guillet, P. R. Selvakannan, H. Remita, B. Palpant, *J. Phys. Chem. C* **2015**, *119*, 7416.
- [51] G. Della Valle, F. Scotognella, A. R. S. Kandada, M. Zavelani-Rossi, H. Li, M. Conforti, S. Longhi, L. Manna, G. Lanzani, F. Tassone, *J. Phys. Chem. Lett.* **2013**, *4*, 3337.
- [52] M. Born, E. Wolf, *Principles of optics: Electromagnetic theory of propagation, interference and diffraction of light*, Elsevier, Berlin **2013**.
- [53] L. Mascaretti, T. Barman, B. R. Ricchi, F. Münz, A. L. Bassi, Š. Kment, A. Naldoni, *Appl. Surf. Sci.* **2021**, *554*, 149543.
- [54] S. Anisimov, B. Kapeliovich, T. Perelman, *Zh. Eksp. Teor. Fiz* **1974**, *66*, 375.
- [55] P. B. Allen, *Phys. Rev. Lett.* **1987**, *59*, 1460.
- [56] F. Caruso, D. Novko, *Adv. Phys.: X* **2022**, *7*, 2095925.
- [57] A. Jain, A. J. McGaughey, *Phys. Rev. B* **2016**, *93*, 081206.
- [58] W. Lengauer, S. Binder, K. Aigner, P. Ettmayer, A. Guillo, J. Debuigne, G. Groboth, *J. Alloys Compd.* **1995**, *217*, 137.
- [59] P. J. Linstrom, W. G. Mallard, *J. Chem. Eng. Data* **2001**, *46*, 1059.
- [60] A. Kanavin, I. Smetanin, V. Isakov, Y. V. Afanasiev, B. Chichkov, B. Wellegehausen, S. Nolte, C. Momma, A. Tünnermann, *Phys. Rev. B* **1998**, *57*, 14698.
- [61] R. Rosei, *Phys. Rev. B* **1974**, *10*, 474.
- [62] F. Masia, W. Langbein, P. Borri, *Phys. Rev. B* **2012**, *85*, 235403.
- [63] C. Thomsen, H. T. Grahn, H. J. Maris, J. Tauc, *Phys. Rev. B* **1986**, *34*, 4129.
- [64] H. Guo, W. Chen, Y. Shan, W. Wang, Z. Zhang, J. Jia, *Appl. Surf. Sci.* **2015**, *357*, 473.
- [65] W. M. Haynes, *CRC handbook of chemistry and physics*, CRC Press, Boca Raton **2016**.
- [66] A. Kozma, *Technol. Transfer Fundam. Princip. Innov. Tech. Solutions* **2020**, *4*, 14.
- [67] S. Dal Conte, M. Conforti, D. Petti, E. Albisetti, S. Longhi, R. Bertacco, C. De Angelis, G. Cerullo, G. Della Valle, *Phys. Rev. B* **2014**, *89*, 125122.
- [68] A. Marini, M. Conforti, G. Della Valle, H. Lee, T. X. Tran, W. Chang, M. Schmidt, S. Longhi, P. S. J. Russell, F. Biancalana, *New J. Phys.* **2013**, *15*, 013033.
- [69] T. Namazu, S. Inoue, H. Takemoto, K. Koterazawa, *IEEJ Trans. Sens. Micromachines* **2005**, *125*, 374.